TEM imaging of clustered Au substitutional impurities in $YBa_2Cu_3O_{6.9}$

B.G. Storey [a,*], M.A. Kirk [b], L.D. Marks [a]

[a] Materials Science and Engineering, Northwestern University, Evanston, IL 60208, USA
[b] Materials Science Division, Argonne National Laboratory, Argonne, IL 60439, USA

Abstract

Evidence for clustering of Au impurity atoms into randomly distributed 1–2 nm rods is presented for $YBa_2Cu_3O_{7-\delta}$ ($\delta < 0.1$) grown by the self-flux technique in Au crucibles. Electron-diffraction patterns show very weak diffuse streaks along $\langle 100 \rangle$ and $\langle 010 \rangle$, and these streaks persist over several degrees of tilt indicating rod-like defects. Multislice image simulations, including the effect of amorphous carbon, for a variety of defect types are compared to high-resolution images. The model that best fits the experimental data is defects made up of 3–4 unit cell long Au–O vacancy rods along $\langle 010 \rangle$ and Au–O interstitial rods along $\langle 100 \rangle$. In light of flux-pinning data comparing YBCO crystals with and without Au doping, these defects should be considered as flux-pinning sites in as-grown Au doped crystals.

1. Introduction

A great deal of attention has been directed towards determining the native defect structures present in $YBa_2Cu_3O_{7-\delta}$ (YBCO), most of which has been concerned with the long-range ordering in highly O deficient samples (theoretical predictions by de Fontaine et al. [1] and experimental evidence by Beyers et al. [2] and Werder et al. [3]). Little has been done to determine the structure of O vacancy and cation impurity clusters or the role of such defects as weak flux-pinning centers in crystals near full oxygenation. Reyes-Gasga et al. [4] did observe weak diffuse streaks in transmission electron-diffraction patterns from sintered samples near full oxygenation, and proposed a 2–4 O vacancy clustering model. However, there was no discussion of possible cation impurities and there were no simulations of the proposed defect model.

A large portion of impurities in single crystals results from the environment in which they are grown. A common method for growing YBCO single crystals is the self-flux method in Au crucibles [5]. Neutron and X-ray diffraction experiments [6] show that at elevated temperatures Au exclusively substitutes for Cu in the CuO chain plane, up to 3 wt.% (10 at.% per formula unit) after which Au precipitates begin to form. Neutron activation analysis on crystals grown at Argonne National Laboratory revealed that the Au concentrations were typically about 8–10 at.% [7]. There are two main advantages to growing YBCO in Au crucibles: an increase in T_c of $\simeq 1$ K and typically larger crystals [6]. Thus a lot of attention was given to Au doped materials as all other cation doping leads to a de-

---

* Corresponding author.

crease in T_c. However, most of this attention was directed towards the unit-cell distortion, and also to the valence variation of Au and copper as a function of O content [8].

This paper provides a comparison of high-resolution electron microscope (HREM) images and diffraction patterns of YBCO with corresponding simulations for several point-defect cluster models.

The best model has randomly distributed rod-like defects consisting of Au^+ and O vacancies along $\langle 010 \rangle$ and Au^{3+} and O interstitials along $\langle 100 \rangle$. Other point-defect cluster models are presented and shown to be inadequate. The existence of these defects is supported by the flux-pinning data of Viswanathan et al. [9], who reported a higher critical current in Au doped YBCO crystals than in pure
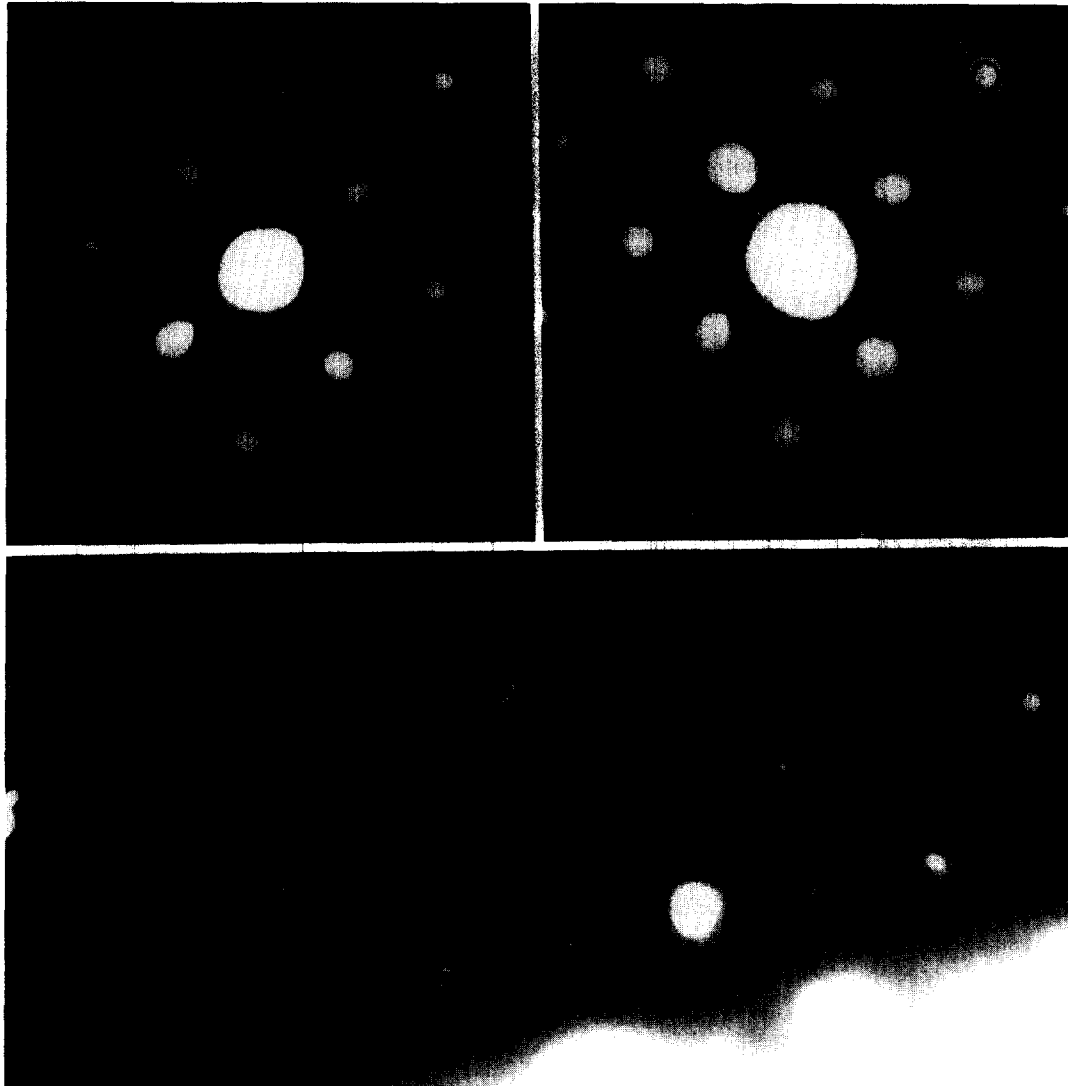

Fig. 1. Electron-diffraction patterns down the $\langle 001 \rangle$ axis from the same area of an untwinned region: (a) room temperature, (b) 88 K. There are diffuse streaks along $\langle 010 \rangle$ and $\langle 100 \rangle$ at both temperatures. The insets show constant intensity contour plots. Figure 1(c) is of a different region taken at room temperature and is tilted approximately seven degrees from the $\langle 001 \rangle$ axis. Note that the diffuse streaks persist at large tilts indicating a diffuse wall of intensity in reciprocal space. The inset shows the intensity profile along the line in the figure.

YBCO. This implies a pinning site that may be related to the presence of Au; we will return to this later.

2. Experimental methods

Single crystals of YBCO were grown, at Argonne National Laboratory, in Au crucibles by the self-flux method [5] and had typical sizes of $1 \times 1 \times 0.05$ mm^3. The crystals were oxygenated in flowing oxygen at 480°C for three days and then furnace cooled to 420°C and held there for another five days and finally furnace cooled to room temperature. A low-field SQUID magnetometer was used to determine T_c values, which were over 90.5 K with a transition width of less than 1 K. Energy dispersive X-ray spectroscopy (EDS) analysis, performed in both a scanning and a transmission electron microscope, verified a 2.5 wt.% Au content which agrees with results by neutron activation.

TEM samples were prepared by dispersing a crushed crystal in two drops of anhydrous methanol onto a clean 1000 mesh TEM grid, and immediately inserting into a TEM for analysis. This procedure resulted in minimal sample damage compared to ion milling or chemical polishing, and reduced the exposure to water and air. All TEM data were collected at 100 keV which is below the threshold voltage for damage of ≈ 130 keV [10,11]. HREM images were obtained using a Hitachi H-9000, while diffraction patterns at room temperature and 88 K were obtained using a Philips CM 30 with a Gatan double tilt liquid-helium holder.

An Optronics P1000 densitometer was used to digitize the negatives to eight bits with a linear distribution of optical densities between zero and two. The images were then processed with SEMPER software on Apollo workstations. A Wiener filter [12] was used to remove the shot noise from the images. This was done by estimating the noise in the power spectrum and then removing it from the amplitude component of the Fourier transform.

3. Experimental results

The first evidence we obtained for defect clustering in Au doped YBCO was diffuse streaks in
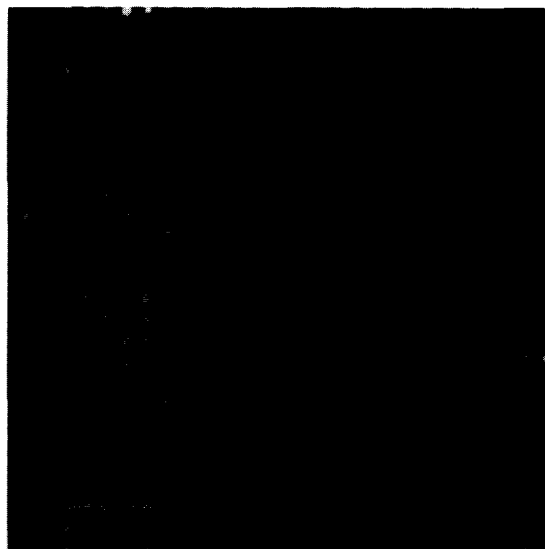

Fig. 2. High-resolution electron micrograph of $YBa_2Cu_3O_{7-\delta}$ on the $\langle 001 \rangle$ axis. Observe the non-uniform variation in intensity over very short ranges. This variation would not be present in a perfect crystalline material.

high-resolution electron-diffraction patterns of long exposure. Figs. 1(a) and (b) are $\langle 001 \rangle$ zone axis diffraction patterns from the same area of a region without twin boundaries at room temperature and 88 K, respectively. One finds extremely weak diffuse streaks of intensity along $\langle 100 \rangle$ and $\langle 010 \rangle$ that are present at low temperatures thereby eliminating thermal diffuse scattering as their source. The diffraction pattern is from an untwinned region, therefore the defects must lie along both $\langle 100 \rangle$ and $\langle 010 \rangle$. These streaks are also maintained upon tilting the crystal seven degrees off the zone axis as shown in Fig. 1(c), therefore, they must be thick walls of diffuse intensity in reciprocal space resulting from short rod-like defects in real space. An intensity profile along the straight line indicated in Fig. 1(c) clearly shows the presence of the aforementioned streaks.

A typical high-resolution image in Fig. 2 shows a very local non-periodic variation in intensity that is not seen in an image of a perfect crystalline material. The area of Fig. 2 is approximately 50 nm from the edge of the sample, therefore the intensity variation is not due to a high thickness ratio of amorphous carbon to sample. This variation in intensity was used to match against the simulated images of differ-
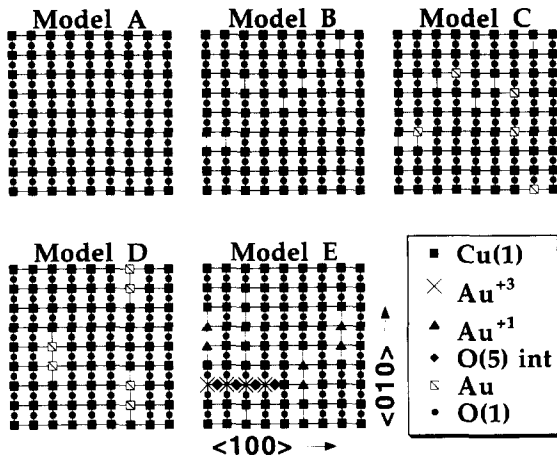
Fig. 3. Array of 8×8 unit cells showing one of the 12 CuO chain planes used for each of the five models presented. The defects are randomly distributed in three dimensions and thus the stoichiometry is determined over all 12 layers and not by the single planes shown.

ent point defect cluster models. These models, presented in Section 4, assume the defects are randomly positioned and are of a high enough density such that they will overlap in the image and therefore individual defects cannot be discerned.

4. Defect models and image simulations

Many different types of defects were modeled and simulated for comparison with the experimental images and diffraction patterns. The defects were randomly distributed in an $8 \times 8 \times 12$ array of unit cells with a thickness of 140 Å or twelve unit cells along $\langle 001 \rangle$; defects were restricted to the CuO chain plane. Fig. 3 shows one of the twelve different CuO chain planes for each of the five models presented in this paper. In describing the defect model, this paper uses the nomenclature for atom sites in the YBCO unit cell given by Jorgensen et al. [13]. Several assumptions were made in the defect models: O vacancies were on the O(1) chain site, Au substituted for the Cu(1) chain position, the Au concentration was 3% of the total Cu(1) or 1 Au/11 unit cells and O vacancy concentration was 1 vacancy/10 unit cells (i.e. $\delta = 6.9$).

The defect models presented below primarily consider small rod-like defects and not square or triangular shaped defect clusters. This is based on tests using a 2D projection of model defects randomly positioned in 3D. The number of defects per unit area in a 2D projection is simply a function of the thickness along the projected direction, and the defect density. By combining a defect size of a few unit cells, based on electron-diffraction data, and an O stoichiometry of $\delta = 6.9$, an appropriate defect density can be calculated. Defects of intensity value equal to one were randomly added to an image of an original value equal to zero, and summed. After the correct number of defects had been generated, a Fourier transform was performed. A variety of defect shapes and orientations was attempted and the Fourier transform results are as follows: point defects yielded a homogeneous diffuse background, small square defect clusters yielded decaying Bessel functions perpendicular to the defect edges, and rod-like defects gave weak streaks similar to those in the diffraction pattern. It is based upon this statistical analysis that rod-like shapes were chosen for the defect modeling.

As mentioned, five simulated models are provided for comparison with the experimental images. Model A is a fully oxygenated defect-free YBCO crystal and shows the perfectly repetitive nature of the image intensity. Model B has random single O vacancies and no Au, while model C takes the same O vacancies as in model B and randomly substitutes Au for Cu(1). These two models represent a widely held model for the state of YBCO. Model D combines Au and O vacancies into short rods along $\langle 010 \rangle$.

Model E which will be shown to fit the experimental data best combines three types of 1–2 nm defect rods. The main feature is Au rods along $\langle 010 \rangle$ and $\langle 100 \rangle$. The association of Au with O vacancies or O interstitials is based on the need to balance local charge. According to Eibshutz et al. [8], Au is completely trivalent in a fully oxygenated sample and completely monovalent in samples where $\delta = 1$, with a portion of each state for intermediate oxygen stoichiometries. They reported that for $\delta = 0.1$ there should be approximately sixty percent Au^{3+} and forty percent Au^{+}. It was also stated that due to the higher charge of Au^{3+} compared to Cu^{2+} (which has a radius of 0.85 Å similar to 0.73 Å for Cu^{2}) it attracts O into the system. Thus an O interstitial may

preferentially sit next to an Au^{3+}, while O vacancies would tend to sit next to the much larger (radius 1.37 Å) Au^+. This led to a model of trivalent Au sharing O interstitials in the normally vacant O(5) site and monovalent Au sharing O vacancies in the O(1) site.

The samples analyzed had a thin covering of amorphous material; consequently, the possibility that this contamination was the reason for the intensity variation in the HREM images had to be tested. The width of the amorphous material at the sample's edge was approximately 30 Å, therefore three thicknesses: 7.8, 19.5, and 39 Å of amorphous carbon were added to the top and bottom surfaces of the simulated material for models A, C and E. Following the technique of Paciornik et al. [14], carbon atoms were positioned randomly in 3.85 Å boxes with the only restriction being that no two carbon atoms could be closer than the carbon atom's diameter.

The defocus and convergence were determined from power spectra of the sample's small amorphous edge. The microscope parameters used were: Cs = 1.75 mm, convergence = 1.5 mrad, energy spread = 8 nm, isotropic vibration = 1 Å, and a voltage of 100 keV. Multislice simulations were performed on Apollo workstations using Northwestern University Multislice and Imaging Software (NUMIS) and the
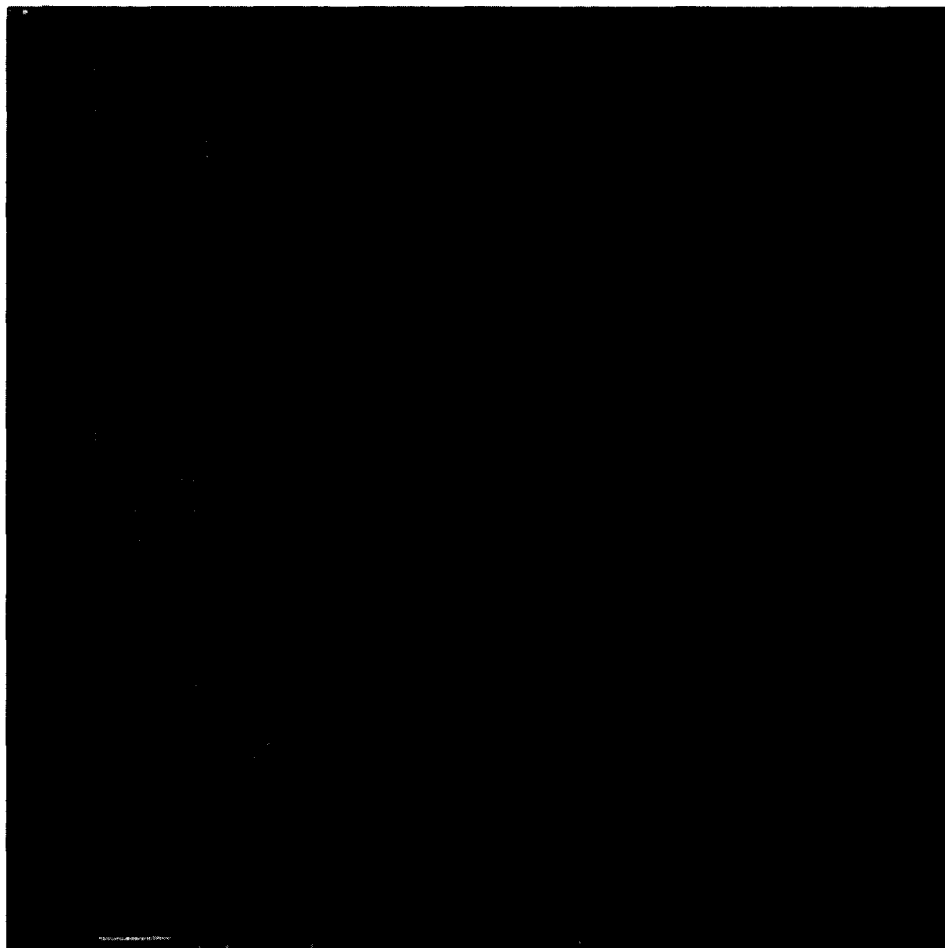

Fig. 4. High-resolution image (100 nm underfocus) down the $\langle 001 \rangle$ zone axis with simulations of defect models A–E inserted. Models A, C and E have four simulations in row representing: 0, 7.8, 19.5, and 39 Å of amorphous carbon added to the top and bottom surfaces of the simulated material. Notice the directionality of the dark streaks in the simulation of model D, which is not found experimentally.

simulated images were pasted onto the experimental images using SEMPER software. The simulated mean intensity was set equal to the mean intensity of the local experimental area into which the simulated image was pasted.

5. Comparison of experimental and simulated results

Three members of a through focal series, Figs. 4–6, are presented as we feel that at least this many are required to match experimental to simulated images. Multislice image simulations of the five models (A–E) are inserted into each experimental image. Note that models A, C and E are simulated with: 0, 7.8, 19.5 and 39 Å of amorphous carbon added to the top and bottom surfaces. The top row (model A) of simulations is of a fully oxygenated Au free material and shows the uniform contrast variation in a perfect crystal. This model does show some variation in the contrast similar to that seen in the experimental image as an increasing amount (left to right) of carbon is added. However, to generate a comparable intensity variation at least 19.5 Å of carbon is required and this amount of carbon starts to introduce systematic contrast variations in the image that do not match the experimental images at certain
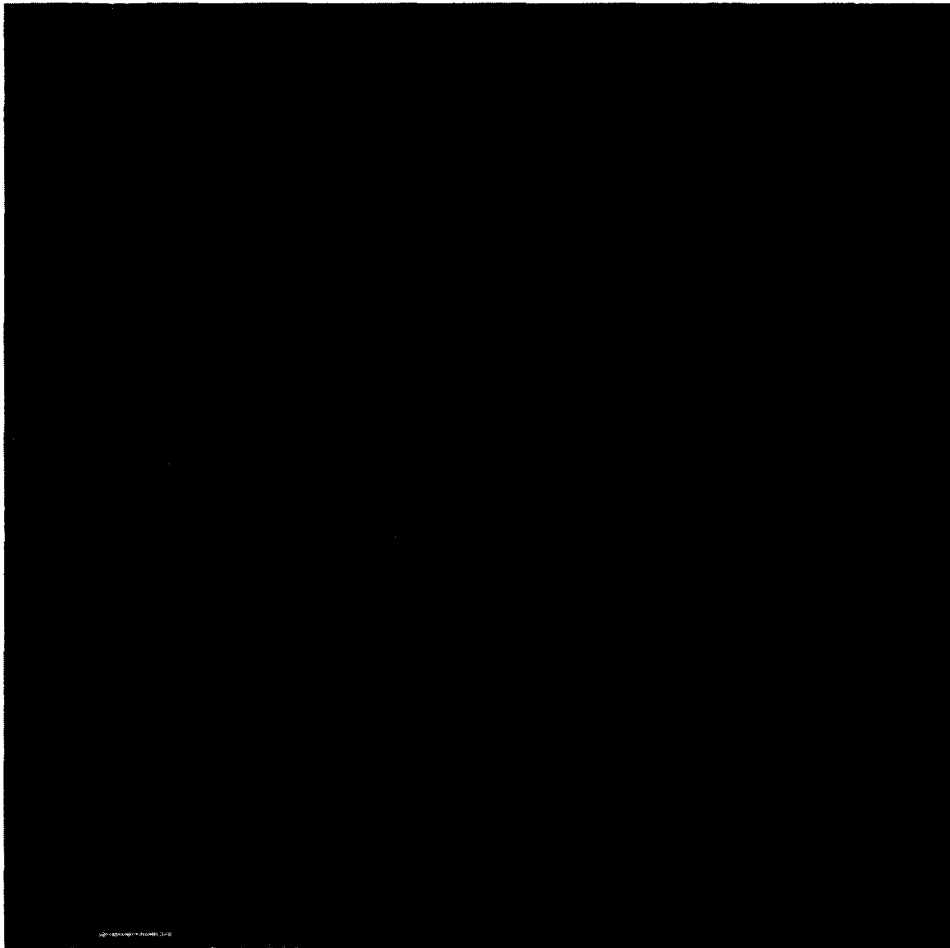

Fig. 5. High-resolution image (132 nm underfocus) down the ⟨001⟩ zone axis with simulations of defect models A–E inserted. Models A, C and E have amorphous carbon added to the top and bottom surfaces as explained in the caption for Fig. 4.

defoci, see for example Fig. 6. Therefore, carbon alone cannot explain the contrast variation.

The second row (model B) represents random single O vacancies and still no Au doping. This simulation also fails to generate the required contrast variation. Many attempts were made to obtain the contrast variation observed by using O vacancies clusters of different size and shape; however, a reasonable match was never obtained. It is understandable that the simulations of models based solely on oxygen-vacancy defects do not fit the experimental images as the EDS analysis showed a consistent presence of 2.5 wt.% Au. Therefore, as Au has a

much higher scattering factor for electrons than copper, any proper model must include Au.

The bottom three rows of simulations in Figs. 4–6 represent defect models C–E and all combine O vacancies and Au atoms. All defect models containing Au produced a significant variation in contrast. However, many of these models generated a directional contrast variation that did not match the experimental images found as evidence for by the simulation in the fourth row (model D). This model had defect rods only along ⟨010⟩ and thus the intensity tends to vary along ⟨100⟩ differently than along ⟨010⟩. The third row (model C) of simulations

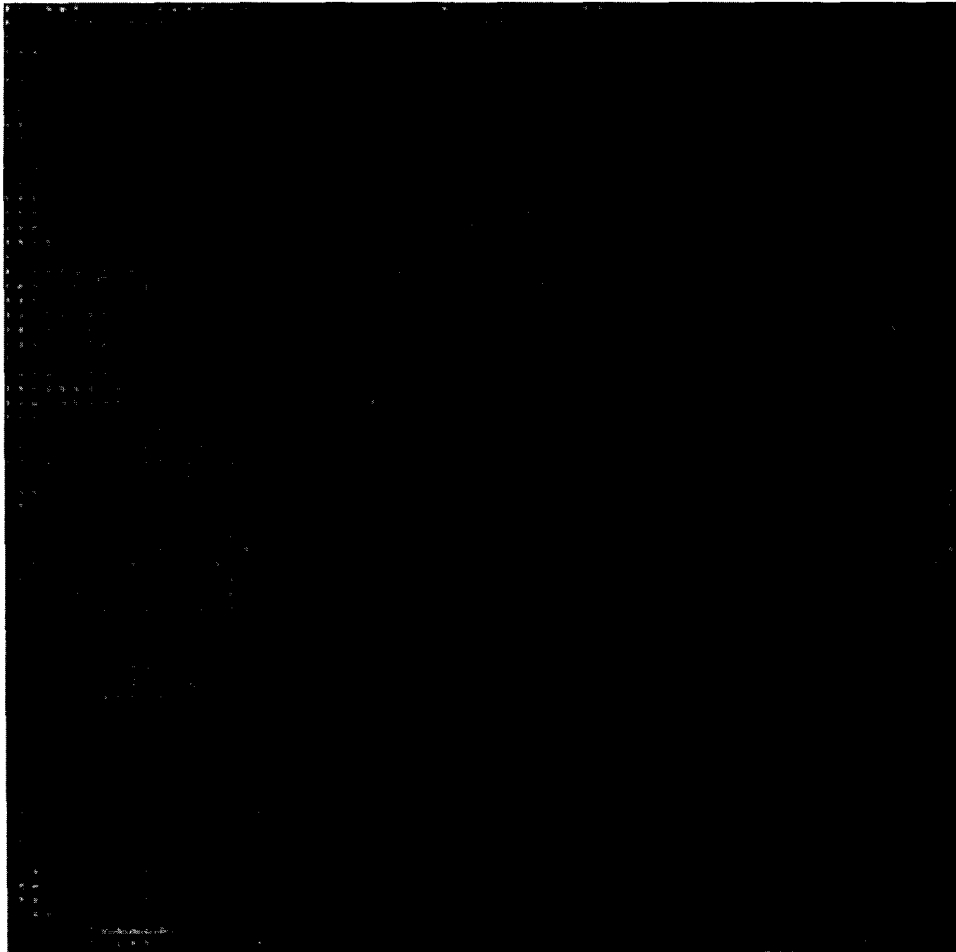
Fig. 6. High-resolution image (214 nm underfocus) down the ⟨001⟩ axis with simulations of defect models A–E inserted. Models A, C and E have amorphous carbon added to the top and bottom surfaces as explained in the caption for Fig. 4. Notice that with increasing amorphous carbon there is an increasingly evident periodic dark contrast not seen in the experimental image.
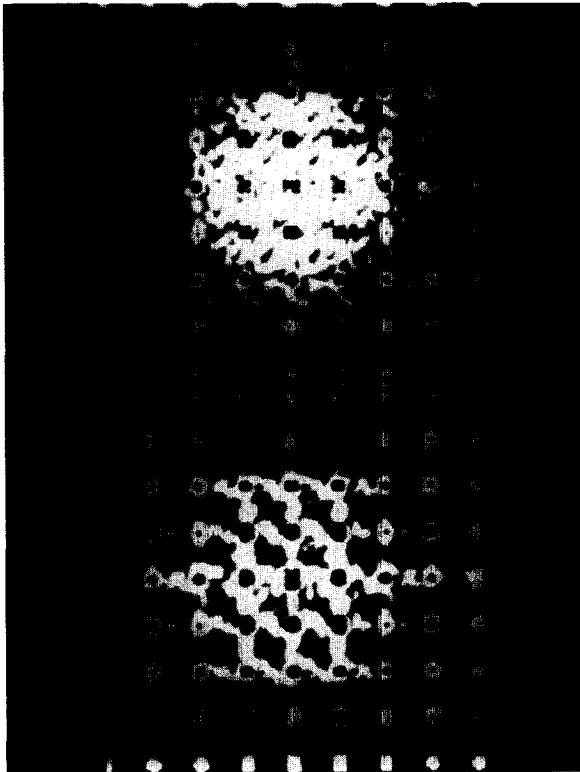
Fig. 7. Simulated electron micro-diffraction patterns for (a) Model C and (b) Model E. Note that the diffuse intensity is homogeneous for Model C but is streaked for Model E. By comparison of these streaks to those in the experimental diffraction patterns shown in Fig. 1(c) it is evident that model E remains plausible while model C fails.

represents single O vacancies not correlated with the single Au atoms and works reasonably well for the image simulations; however, as shown in the diffraction simulations, Figs. 7(a) and (b), it does not generate the diffuse streaking. The fifth row (model E) represents the model that best fits both the images and the diffraction patterns. Note that the simulations of models C and E do not require carbon contamination layers to obtain a good fit.

Micro-diffraction pattern simulations, Figs. 7(a) and (b), are needed to distinguish whether model C or E was correct. It is important to realize that the mean level of each pattern is the same. The pattern for model C shows a homogeneous spread in the diffuse intensity while the simulation for model E has the required streaks along both the $\langle 100 \rangle$ and $\langle 010 \rangle$. The diffuse intensity in the simulated streaks

is 5–6 orders of magnitude less than the intensity at the bulk reflections, and this explains the very weak intensity in the experimental electron-diffraction pattern. Electron-diffraction patterns were simulated for many of the other models including those not presented in this paper. Micro-diffraction simulations of models containing rods of O vacancies without any Au did produce the required diffraction streaks; however, the diffuse intensity was 7–8 orders of magnitude less than the bulk reflections, which is probably too weak to obtain in an experimental electron-diffraction pattern.

6. Discussion

The use of a TEM to investigate the nature of point-defect clusters has been mostly ignored. However, our multislice simulations show the effect of random clusters, of sufficient density and scattering power, should be observable in both HREM images and diffraction patterns. Regrettably, this technique of combining HREM and electron diffraction cannot reliably discriminate between model E and a similar model (not presented) in which the O interstitials on the O(5) site between Au^{3+} are removed. The latter model would then have short Au rods along both $\langle 100 \rangle$ and $\langle 010 \rangle$ without any O between the Au atoms. The reason for including O defects in the Au rods is for local charge balance. As mentioned previously, Eibschütz et al. [8] reported the presence of Au^{3+} and Au^{+} on Cu^{2+} sites with a $Au^{3+}:Au^{+}$ dependence on O concentration. With Au^{+} being much larger and more negative than Cu^{2+}, it stands to reason that an O vacancy may sit next to Au^{+}; similarly, Au^{3+} is about the same size and is more positive than Cu^{2+} and an O interstitial may sit next to Au^{3+}.

The defects proposed in this paper must be considered as possible flux-pinning sites in as-grown Au doped YBCO, even though they lie in the CuO chain plane and not the CuO_2 plane. This is supported by the work of Viswanathan et al. [9] comparing crystals grown in Au versus ZrO_2 crucibles. They showed a flux-pinning disparity that suggested the existence of as-grown defects in the Au doped YBCO crystals. The ZrO_2 grown crystals are almost free of cation doping as Zr is less invasive in YBCO than Au, and

had consistently lower critical currents as a result of fewer flux-pinning defects. The same study then irradiated these crystals with 3.5 MeV protons to a fluence of 1×10^{16} p cm^{-2} and found that the Au doped crystals then had the lower critical currents. These results can be explained by an as-grown defect acting prior to irradiation as a flux-pinning center and during irradiation to prohibit the formation of larger irradiation defects by inhibiting the coalescence of the many point defects generated by the irradiation damage.

7. Conclusion

The combination of careful diffraction analysis, high-resolution imaging and multislice image simulations allows for the investigation of randomly distributed small clusters of point defects. This holds true even for clusters dispersed in a heavy cation matrix and in the case of single YBCO crystals grown in Au crucibles yields a model for the clustering of Au substituted for Cu(1) and O point defects into 1 nm rods in the CuO chain plane. Oxygen interstitials, O(5) site, combine with Au^{3+} along the $\langle 100 \rangle$, while O vacancies combine with Au^{+} along the $\langle 010 \rangle$.

The defects proposed here are possible flux-pinning sites in as-grown Au doped YBCO crystals. It would be of interest to investigate the flux-pinning dependence on variable Au doping of YBCO crystals grown in ZrO$_2$ crucibles. This would solidify the hypothesis that the Au is responsible for the flux pinning.

The benefits of YBCO grown in Au crucibles are increased crystal size, T_c, and improved flux pinning. However, these benefits must be balanced against the knowledge that the Au does form O related defects and does not remain inert in the system. Therefore, research on the basic properties of YBCO should not be performed on YBCO doped with Au unless it is certain that the effect of the Au can be taken into account.

Referneces

[1] D. de Fontaine, G. Ceder and M. Asta, Nature (London) 343 (1990) 544.
[2] R. Beyers, B.T. Ahn, G. Gorman, S.S.P. Parkin, M.L. Ramirez, J.E. Vazquez, T.M. Gür and R.A. Huggins, Nature (London) 340 (1989) 619.
[3] D.J. Werder, C.H. Chen, R.J. Cava and B. Barlogg, Phys. Rev. B 37 (1988) 2317.
[4] J. Reyes-Gasga, T. Krekels, G. Van Tendeloo, J. Van Landuyt, A. Amelinckx, W.H.M. Bruggink and H. Verweij, Physica C 159 (1989) 831.
[5] D.L. Kaiser, F. Holtzberg, M.F. Chisholm and T.K. Worthington J. Cryst. Growth 85 (1987) 593.
[6] M.Z. Cieplak, G. Xiao, C.L. Chien, A. Bakhshai, D. Artmowicz, W. Bryden, J.K. Stalick and J.J. Rhyne, Phys. Rev. B 42 (1990) 6200.
[7] M.C. Frischherz, private communication.
[8] M. Eibschütz, M.E. Lines, W.M. Reiff, B. van Dover, J.V. Waszczak, S. Zahurak and R.J. Felder, Appl. Phys. Lett. 62 (1993) 1827.
[9] H.K. Viswanathan, Phys. Rev. B, submitted.
[10] S.N. Basu, T.E. Mitchell and M. Nastasi, J. Appl. Phys. 69 (1991) 3167.
[11] M.A. Kirk, M.C. Baker, J.Z. Liu, D.J. Lam and H.W. Weber, Mater. Res. Soc. Symp. Proc. 99 (1988) 209.
[12] L.D. Marks, to be submitted.
[13] J.D. Jorgenson, B.W. Veal, W.K. Kwok, G.W. Crabtree, A. Umezawa, L.J. Nowicki and A.P. Paulikas, Phys. Rev. B 36 (1987) 5731.
[14] S. Paciornik, R. Kilaas and U. Dahmen, Ultramicroscopy 50 (1993) 255.